Optically-Controlled "Living Electrodes" with Long-Projecting Axon Tracts for a Synaptic Brain-Machine Interface

Dayo O. Adewole[1,2,3,4], Laura A. Struzyna[1,2,3,4], James P. Harris[1,2], Ashley D. Nemes[1,2], Justin C. Burrell[1,2,3], Dmitriy Petrov[1,2], Reuben H. Kraft[5], H. Isaac Chen[1,2], Mijail D. Serruya[2,6], John A. Wolf[1,2], D. Kacy Cullen[1,2,3,4,*]

(1) Center for Brain Injury & Repair, Department of Neurosurgery, Perelman School of Medicine, University of Pennsylvania, Philadelphia, PA, 19104, USA;
(2) Center for Neurotrauma, Neurodegeneration & Restoration, Corporal Michael J. Crescenz Veterans Affairs Medical Center, Philadelphia, PA, 19104, USA;
(3) Department of Bioengineering, School of Engineering and Applied Science, University of Pennsylvania, Philadelphia, PA, 19104, USA;
(4) Center for Neuroengineering & Therapeutics, University of Pennsylvania, Philadelphia, PA, 19104, USA
(5) Computational Biomechanics Group, The Pennsylvania State University, University Park, PA, 16802, USA;
(6) Department of Neurology, Thomas Jefferson University, Philadelphia, PA, 19107, USA.

Number of text pages: 11 Number of Figures: 7+ 2 Supplemental

*Corresponding author:
D. Kacy Cullen, Ph.D.
105E Hayden Hall/3320 Smith Walk
Philadelphia, PA 19104
Ph: 215-746-8176 Fx: 215-573-3808
Email: dkacy@pennmedicine.upenn.edu

Summary

Achievements in intracortical brain-machine interfaces are compromised by limitations in long-term performance and information transfer rate. A biological intermediary between devices and the brain based on synaptic integration may offer a specificity and permanence that has eluded neural interfaces to date. Accordingly, we have developed the first "living electrodes" comprised of implantable axonal tracts protected within soft hydrogel cylinders to enable biologically-mediated monitoring and modulation of brain activity. Here we demonstrate the controlled fabrication, rapid axonal outgrowth, reproducible cytoarchitecture, and axonal conduction of these engineered constructs *in vitro*. We also present simultaneous optical stimulation and recording of neuronal activity *in vitro*, transplantation in rat cortex, and their survival, integration, and activity over time *in vivo* as a proof-of-concept for this neural interface paradigm. The creation and functional validation of living electrodes is a critical step towards developing a new class of neural interfaces using targeted, synaptic-based integration with native circuitry.

Keywords

Neuromodulation; living scaffolds; neural tissue engineering; cell transplant; biomaterials; regeneration; brain-computer interface; neurodegeneration; axon pathfinding; synapse

Introduction

Brain-machine or brain-computer interfaces (BMIs/BCIs) transmit information between the nervous system and an external device. These technologies have been applied to investigate fundamental neural processes, operate prostheses, and restore functions lost to neural injury, neurodegeneration, or disease[1,2]. Patients have also used BCIs to restore hearing, control computers, and drive external stimulation of their own muscles[2,3]. While BCIs offer a significant opportunity to treat a range of conditions, several issues have limited their widespread deployment. Broadly, implantable BCIs use inorganic microelectrodes to stimulate or record from the brain[3]. These microelectrodes often exhibit diminished performance over time due to biotic (inflammation, neuronal loss, and glial scarring) and abiotic (biostability issues including decreasing impedance due to loss of insulation, mechanical failure) factors, impeding recording quality[3–8]. BCIs for sensory input and similar technologies for neuromodulation – such deep brain stimulation (DBS) – use electrical stimulation to modulate neuronal activity. However, since electrode charge can spread over a large tissue volume, the ability to target specific neurons or neuronal subtypes (e.g. excitatory vs. inhibitory neurons) is limited[9]. Distinct cell types may be targeted with greater specificity by using optogenetics to activate genetically modified neurons via spatial distribution of light. However, the optogenetic wavelengths are scattered by tissue, thereby blocking precise stimulation of subsets of neurons more than a few hundred microns deep[10]. Implantable optical fibers, lenses, or micro-LEDs have been used, yet performance over time is limited by the foreign body response and/or overheating of surrounding tissue[11,12]. Further, the longevity and immune response in humans is unknown for virally transduced optogenetic proteins. Finally, across electric and/or optical input-output paradigms, the information transfer bandwidth limits the quality of the neural interface. Moving forward, the ideal BCI should employ a precise, stable, and robust interface for modulating or monitoring the nervous system.

To address these limitations, we have developed micro-Tissue Engineered Neural Networks (μTENNs). These precisely formed, living constructs comprise discrete population(s) of neurons connected by long bundles of axons within microscopic hydrogel cylinders ("micro-columns") (Figure 1)[13,14]. μTENNs were originally developed to reconstruct lost or damaged neuroanatomy following brain injury, and previously demonstrated neuronal survival, maintenance of axonal architecture, and synaptic integration with host cortical neurons following targeted microinjection into rats[13,14]. Here, we adapt this approach to provide an entirely new neural pathway between the brain and external devices through synaptic-based inputs to and outputs from the nervous system[13–15]. Our efforts to advance the μTENN technology as a "living

electrode" may uniquely address challenges in current BCIs (Figure 1J). In this radical paradigm, the µTENN is implanted at a predetermined depth to synaptically integrate with local neural circuitry. Neural activity or stimulation is transferred via the engineered axonal tracts within the micro-column to/from inorganic components on the brain surface (Figure 1J). The segregation of biological and inorganic material may ameliorate the foreign body response and improve long-term stability. Moreover, the ability to control the neuronal phenotype of the µTENN provides specificity in targeting subsets of neurons, allowing for a biologically-based, highly selective, and potentially permanent neural interface. The present work details the fabrication and characterization of next-generation axon-based µTENNs *in vitro*, including growth, viability, maturation, and structure. We also demonstrate fully light-based input-output *in vitro* as well as optically-based output following implantation *in vivo* as proof-of-concept for this neural interface paradigm, as well as µTENN survival and integration in the rodent cortex.

Methods

All procedures were approved by the Institutional Animal Care and Use Committees at the University of Pennsylvania and the Michael J. Crescenz Veterans Affairs Medical Center and adhered to the guidelines set forth in the NIH Public Health Service Policy on Humane Care and Use of Laboratory Animals (2015).

Cortical Neuron Isolation and Culture

Neural cell isolation and culture protocols are similar to that of published work[13,14]. Briefly, timed-pregnant rats were euthanized, and the uterus removed. Embryonic day 18 fetuses were transferred from the uterus to cold HBSS, wherein the brains were extracted and the cerebral cortical hemispheres isolated under a stereoscope via microdissection. Cortical tissue was dissociated in 0.25% trypsin + 1mM EDTA at 37˚C, after which the trypsin/EDTA was removed and replaced with 0.15 mg/ml DNase in HBSS. Dissociated tissue + DNase was centrifuged for 3 min at 3000 RPM before the DNase was removed and the cells re-suspended in neuronal culture media, composed of Neurobasal® + B27® + Glutamax™ (ThermoFisher) and 1% penicillin-streptomycin.

Micro-Tissue Engineered Neural Network (µTENN) Fabrication

µTENNs were constructed in a three-phase process (Figure 1A-C). First, agarose micro-columns of a specified geometry (outer diameter (OD), inner diameter (ID), and length) were formed in a custom-designed acrylic mold as described in earlier work (Figure 1A)[16]. The mold is an array of cylindrical channels that allow for the insertion of acupuncture needles (Seirin, Weymouth, MA) such that the needles are concentrically aligned within the channels. The mold has been fabricated with more precise machining equipment relative to earlier work to better ensure concentric tolerance of the needles and channels. Molten agarose in Dulbecco's phosphate buffered saline (DPBS) was poured into the mold-needle assembly and allowed to cool (agarose: 3% weight/volume). Once the agarose solidified, the needles were removed and the mold disassembled, yielding hollow agarose micro-columns with a specific outer diameter equal to the size of the channels and inner diameter equal to the outer diameter of the needles. Micro-columns were sterilized via UV light for 30 min and stored in DPBS to prevent dehydration until needed. For these studies, the mold channels were 398 µm in diameter and the acupuncture needles were 180 µm, resulting in micro-columns with a 398 µm OD and a 180 µm ID. Micro-columns were cut to the desired length for each cohort, as described below.

Next, primary cortical neurons were forced into spheroidal aggregates (Figure 1C). These aggregates provide the necessary architecture for the growth of long axonal fascicles spanning the length of the micro-column. To create aggregates, dissociated cells were transferred to an array of inverted pyramidal wells made in PDMS (Sylguard 184, Dow Corning) cast from a custom-designed, 3D printed mold (Figure 1B). Dissociated cortical neurons were suspended at a density of 1.0-2.0 million cells/ml and centrifuged in the wells at 200g for 5 min. This centrifugation resulted in forced aggregation of

neurons with precise control of the number of neurons per aggregate/sphere (12 µL cell suspension per well). Pyramidal wells and forced aggregation protocols were adapted from Ungrin et al [17].

Finally, micro-columns were removed from DPBS and excess DPBS removed from the micro-column channels via micropipette. Micro-columns were then filled with extracellular matrix (ECM) comprised of 1.0 mg/ml rat tail collagen + 1.0 mg/ml mouse laminin (Reagent Proteins, San Diego, CA) (Figure 1C). Unidirectional or bidirectional µTENNs were seeded by carefully placing an aggregate at one or both ends of the micro-columns, respectively, using fine forceps under a stereoscope, and were allowed to adhere for 45 min at 37˚C, 5% CO_2. To create dissociated µTENNs, dissociated cortical neurons were transferred via micropipette into the ECM-filled micro-column as detailed in prior work [13,14]. µTENNs were then allowed to grow in neuronal culture media with fresh media replacements every 2 days *in vitro* (DIV).

Growth Characterization

Phase-contrast microscopy images of µTENNs in culture were taken at 1, 3, 5, 8, and 10 DIV at 10x magnification using a Nikon Eclipse Ti-S microscope, paired with a QIClick camera and NIS Elements BR 4.13.00. µTENNs were fabricated for classification into one of the following groups: dissociated/2 mm long ($LE_{DISS,2}$) (n = 7), unidirectional/2 mm long ($LE_{UNI,2}$) (n = 6), unidirectional/5 mm long ($LE_{UNI,5}$) (n = 3), bidirectional/2 mm long ($LE_{BI,2}$) (n = 15), bidirectional/3 mm long ($LE_{BI,3}$) (n = 12), bidirectional/5 mm long ($LE_{BI,5}$) (n = 17), bidirectional/7 mm long ($LE_{BI,7}$) (n = 8), bidirectional/9 mm long ($LE_{BI,9}$) (n = 3). Growth rates for each group at specific timepoints were quantified as the change in the length of the longest identifiable neurite divided by the number of days between the current and preceding timepoint. The longest neurites were manually identified within each phase image using ImageJ (National Institutes of Health, MD), and length was measured from the edge of the source aggregate to the neurite tip. To standardize measurements, the edge of the source aggregate identified at 1 DIV was used as the reference point across subsequent timepoints. Growth was measured until axons crossed the length of the column (for unidirectional constructs) or axons crossed the distance between aggregates (for bidirectional constructs). Growth rates were averaged for each timepoint, with the average maximum and minimum growth rates and average crossing time compared across aggregate µTENNs with one-way analysis of variance (ANOVA). Post-hoc analysis was performed where necessary with the Bonferroni procedure ($p<0.05$ required for significance). For reference, planar cultures of cortical neurons (n = 10) were grown in parallel with µTENN cultures, with the longest identifiable neurites measured at 1, 3, and 5 DIV. Single neurites could not be identified at later timepoints due to culture maturation. Axonal outgrowth in planar cultures was taken as the average growth rate across timepoints, which were compared via unpaired t-test. All data presented as mean ± s.e.m.

To identify aggregate-specific growth across the micro-columns, cortical neuronal aggregates were labeled with either green fluorescent protein (GFP) or the red fluorescent protein mCherry via adeno-associated virus 1 (AAV1) transduction (Penn Vector Core, Philadelphia, PA). Briefly, after centrifuging aggregates in the pyramid wells, 1 µL of AAV1 packaged with the human Synapsin-1 promoter was added to the aggregate wells (final titer: ~$3x10^{10}$ viral copies/mL). Aggregates were incubated at 37˚C, 5% CO_2 overnight before the media was replaced twice, after which transduced aggregates were plated in micro-columns as described above, each with one GFP^+ and one $mCherry^+$ aggregate (n = 6). Over multiple DIV, images of the µTENNs were taken on a Nikon A1RSI Laser Scanning confocal microscope paired with NIS Elements AR 4.50.00. Sequential slices of 10-20 µm in the z-plane were acquired for each fluorescent channel. All confocal images presented are maximum intensity projections of the confocal z-slices.

Viability Assessment

To assess neuronal viability, 5-mm long unidirectional (LE_{UNI}) and bidirectional (LE_{BI}) constructs and age-matched planar cultures plated on polystyrene were stained with a calcein-AM/ethidium homodimer-1 (EthD-1) assay (ThermoFisher) at 10 and 28 DIV. Metabolically active cells convert the membrane-permeable calcein AM to calcein, which fluoresces green (λ_{exc} ~495 nm; λ_{em} ~515 nm), while EthD-1 enters membrane-compromised cells and fluoresces red upon binding to nucleic acids (λ_{exc} ~495 nm; λ_{em} ~635 nm). Briefly, cultures were gently rinsed in DPBS. A solution of calcein-AM (1:2000 dilution; final concentration ~2 µM) and ethidium homodimer-1 (1:500; ~4 µM) in DPBS was added to each culture, followed by incubation at 37˚C, 5% CO_2 for 30 min. Following incubation, cultures were rinsed twice in fresh DPBS and imaged at 10x magnification on a Nikon A1RSI Laser Scanning confocal microscope paired with NIS Elements AR 4.50.00. Viability was quantified as the ratio of the total area of calcein-AM-positive cells to the total area of both calcein-AM-positive and ethidium homodimer-positive cells using ImageJ (National Institutes of Health, MD). Sample sizes for each group were as follows: $LE_{UNI,5mm}$ (n = 4, 4); $LE_{BI,5mm}$ (n = 7, 4); planar cultures (n = 9, 5) for 10 and 28 DIV, respectively. All data presented as mean ± s.e.m.

Optical Stimulation, Calcium Imaging, and Optical Recording Analysis

To establish whether µTENNs could be coupled with an all-optical system, cortical neuronal aggregates were transduced with either the genetically encoded fluorescent calcium reporter RCaMP1b for optical output or channelrhodopsin-2 (ChR2) for light-based input, via adeno-associated virus 1 (AAV1) transduction as described above (Penn Vector Core). 5-6 mm-long bidirectional µTENNs were then plated with one “input” (ChR2) aggregate and one “output” (RCaMP1b) aggregate at either end (n = 5). ChR2 and RCaMP have been investigated and used for all-optical electrophysiology *in vitro* with minimal spectral overlap, reducing the likelihood of false positive responses due to stimulation of the input aggregate exciting the output aggregate[18]. At 10 DIV, µTENNs were stimulated via an LED optical fiber positioned approximately 1-3mm above the input aggregate, such that the entire aggregate was illuminated. A Plexon Optogenetic Stimulation System with LED modules for each desired wavelength was used to stimulate the µTENNs (Plexon Inc). Stimulation consisted of a train of ten 100ms pulses (1 Hz) at 465nm, within the excitation spectra of ChR2. Each train was repeated three times for a given LED current amplitude (50, 100, 200, 250, 300 mA); amplitudes corresponded to stimulation intensities of 106, 211, 423, 528, and 634 mW/mm^2 from the tip of the optical fiber. As a control, µTENNs were stimulated as above at 620nm (outside of the excitation spectra of ChR2) at 300 mA/634 mW/mm^2. Recordings of the µTENNs’ output aggregates were acquired at 25-30 frames per second on a Nikon Eclipse Ti microscope paired with an ANDOR Neo/Zyla camera and Nikon Elements AR 4.50.00 (Nikon Instruments).

To verify whether the fluctuations in calcium reporter fluorescence could be associated with synaptic transmission, bidirectional µTENNs 1.0-1.2mm in length were fabricated and transduced with GCaMP6f (n = 3). At 10 DIV, µTENNs were moved to a stage-mounted warming chamber maintaining incubator conditions (37˚C, 5% CO^2) to record fluorescent calcium reporter activity as described above, with acquisition frequencies of 25-30 frames per second. After 30s of recording spontaneous activity, the NMDA receptor antagonist D-APV (50 µM) and AMPA receptor antagonist CNQX (10 µM) were added to the media containing the µTENNs; recordings were then continued for 20min. Subsequently, media containing D-APV and AMPA was removed and replaced with fresh neuronal culture media. µTENNs were kept at 37˚C, 5% CO_2 overnight, after which spontaneous activity was recorded for an additional 60s.

Following optical stimulation and/or recording, regions of interest (ROIs) containing neurons and background ROIs were identified from the calcium recordings. The mean pixel intensities for each ROI were imported into MATLAB for further analysis via custom scripts (MathWorks Inc). Within MATLAB, the background ROI intensity for each recording was subtracted from active ROIs. Ten such ROIs were randomly selected and averaged to obtain a representative fluorescence intensity trace across each

output aggregate. Subsequently, the percent change in fluorescence intensity over time ($\Delta F/F_o$) was calculated for each mean ROI, where ΔF equals ($F_T - F_o$), F_T is the mean ROI fluorescent intensity at time T, and F_o is the average of the lower half of the preceding intensity values within a predetermined sampling window[19]. The peak $\Delta F/F_o$ for each train was averaged per µTENN for each of the given stimulation intensities. The average maximum $\Delta F/F_o$ was then compared across stimulation intensities with a one-way ANOVA, with post-hoc analysis performed where necessary with the Tukey procedure ($p<0.05$ required for significance). Additionally, the peak $\Delta F/F_o$ of the output aggregate under 620nm/control stimulation was compared to that under 465nm stimulation at 300 mA/634 mW/mm^2 using an unpaired t-test ($p<0.05$ required for significance). All data presented as mean ± s.e.m.

Immunocytochemistry

µTENNs were fixed in 4% formaldehyde for 35 min at 4, 10, and 28 DIV (n = 6, 4, and 8, respectively). µTENNs were then rinsed in 1x PBS and permeabilized with 0.3% Triton X100 + 4% horse serum in PBS for 60 min before being incubated with primary antibodies overnight at 4˚C. Primary antibodies were Tuj-1/beta-III tubulin (T8578, 1:500, Sigma-Aldrich) to label axons and synapsin-1 (A6442, 1:500, Invitrogen) to label pre-synaptic specializations. Following primary antibody incubation, µTENNs were rinsed in PBS and incubated with fluorescently labeled secondary antibodies (1:500; sourced from Life Technologies & Invitrogen) for 2h at 18˚-24˚C. Finally, Hoechst (33342, 1:10,000, ThermoFisher) was added for 10 min at 18˚-24˚C before rinsing in PBS. µTENNs were imaged on a Nikon A1RSI Laser Scanning confocal microscope paired with NIS Elements AR 4.50.00. Sequential slices of 10-20 µm in the z-plane were acquired for each fluorescent channel. All confocal images presented are maximum intensity projections of the confocal z-slices.

Cortical Implantation and Intravital Calcium Imaging

As a proof-of-concept for µTENN behavior *in vivo*, bidirectional, approximately 1.5mm-long µTENNs expressing GCaMP were delivered into the brain via stereotaxic microinjection using similar methodology to that described in prior work [13,14]. Male Sprague-Dawley rats weighing 325-350 grams were anesthetized with isoflurane at 1.0-2.0 liters per minute (induction: 5.0%, maintenance: 1-5-2.0%) and mounted in a stereotactic frame. Meloxicam (2.0 mg/kg) and bupivacaine (2.0 mg/kg) were given subcutaneously at the base of the neck and along the incision line, respectively. The area was shaved and cleaned with betadine solution, after which a small craniotomy was made over the primary visual cortex (V1) (coordinates: -5.0mm AP, ±4.0mm ML relative to bregma). µTENNs were loaded into a needle coupled to a Hamilton syringe and mounted onto a stereotactic arm. To deliver the constructs into the brain without forcible expulsion, the needle was mounted on a micromanipulator and slowly inserted into the cortex to a depth of 1.0 mm such that the dorsal µTENN terminal was left ~500 µm above the brain surface. The plunger of the Hamilton syringe was then immobilized, while the needle containing the µTENN was slowly raised. Upon needle removal from the brain, the dorsal aggregate of the µTENN was immersed in artificial cerebrospinal fluid (aCSF) warmed to 37˚ C. To protect the dorsal µTENN terminal and enable imaging of the µTENN and surrounding tissue, 2 PDMS discs (5.0mm outer diameter, 2.0mm inner diameter, 0.35mm thickness) were placed over the craniotomy/µTENN and secured to the skull with cyanoacrylate glue. A 3.0mm-diameter glass coverslip was sandwiched between the 2 discs.

At five and ten days post-implant, animals were again anesthetized and mounted on a stereotactic frame for multiphoton calcium imaging of the implant. µTENNs were imaged on a Nikon A1RMP+ multiphoton confocal microscope paired with NIS Elements AR 4.60.00 and a 16x immersion objective. Recordings of the µTENNs' dorsal aggregates were taken at 3-5 frames per second, similarly to other intravital work[20]. Post-recording, ROIs of µTENN neurons were manually identified, with the mean pixel intensity of each ROI plotted over time. To distinguish neuronal activity from the animal breathing artifact, the fast Fourier transform (FFT) of the mean pixel intensity averaged across 10-15 ROIs was used to identify the frequency peak(s) associated with the observed breathing rate during imaging.

Peaks were identified as frequencies whose amplitudes were 2 standard deviations or more than the average amplitude of the Fourier spectra.

Tissue Harvest and Histology

Post-implant, rats were anesthetized with 150 mg/kg euthasol (Midwest) and transcardially perfused with cold heparinized saline and 10% formalin. After post-fixation of the head overnight, the brain was harvested and stored in PBS to assess µTENN survival and host/µTENN synaptic integration (n = 6). Histology was performed via traditional immunohistology (IHC) and the Visikol clearing method to resolve thicker tissue sections where appropriate.

For traditional IHC, brains were sagittally blocked and cut in 40 µm slices for cryosectioning. For frozen sections, slices were air-dried for 30 minutes, twice treated with ethanol for three minutes, and rehydrated in PBS twice for three minutes. Sections were blocked with 5% normal horse serum (ABC Universal Kit, Vector Labs, cat #PK-6200) in 0.1% Triton-x/PBS for 30-45 minutes. Primary antibodies were applied to the sections in 2% normal horse serum/Optimax buffer for two hours at room temperature. Primary antibodies were chicken anti-MAP2 (1:1000), mouse anti-Tuj1 (1:1000), and mouse anti-synapsin (1:1000). Sections were rinsed with PBS three times for five minutes, after which secondary antibodies (1:1000) were applied in 2% normal horse serum/PBS for one hour at room temperature. Sections were counterstained with DNA-specific fluorescent Hoechst 33342 for ten minutes and then rinsed with PBS. After immunostaining, slides were mounted on glass coverslips with Fluoromount-G mounting media.

In the Visikol method, brains were glued to a vibratome mounting block directly in front of a 5% low EEO agarose post (Sigma A-6103) and placed in PBS surrounded by ice. The brain was cut in 100-200 µm coronal segments with a Leica VT-1000S vibratome until the µTENN implantation site was approximately 1 mm from the cutting face. Subsequently a single 2 mm section containing the microTENN was cut and placed in PBS (frequency setting: 9, speed: 10). The 2 mm brain section was treated at 4°C with 50%, 70%, and 100% tert-butanol, each for 20 minutes. After the ascending tert-butanol steps, the tissue was removed and placed on a kimwipe to carefully remove any excess reagent. Visikol Histo-1 was applied to the sample for 2 hours at 4°C followed by Visikol Histo-2 for 2 hours at 4°C to complete the clearing process. The sample was placed in a petri dish and a hydrophobic well was drawn around the tissue. Fresh Visikol Histo-2 was applied to completely submerge the tissue, which was then covered by a glass coverslip.

Coverslips containing brain slices were imaged on a Nikon A1RMP+ multiphoton confocal microscope paired with NIS Elements AR 4.60.00 and a 16x immersion objective. A 960-nm laser was used to visualize the µTENN containing neurons expressing GFP/GCaMP.

Data Availability

The data that support the findings of this study are available from the corresponding author upon reasonable request.

Results

The objectives of our current efforts were threefold: (1) to reproducibly fabricate “living electrode” µTENNs and characterize their growth, architecture, viability, phenotype, and synaptic functionality, (2) to demonstrate the ability to control and monitor µTENNs via light, and (3) to determine whether transplanted µTENN neurons survive *in vivo* and remain viable and active in the host cortex.

Fabrication and Axonal Outgrowth

In earlier work, µTENNs were seeded with single cell suspensions of primary cortical neurons, which in many cases formed clusters at random sites throughout the micro-column interior (Figure 1). Current-

generation µTENNs were built using cortical aggregates that have been formed prior to plating in the micro-columns, allowing for greater control and reproducibility of the desired cytoarchitecture of discrete somatic and axonal zones (Figure 1). This reproducibility lends itself to consistently creating the desired cytoarchitecture *in vitro*, a necessary step in applying them as living electrodes. Aggregate µTENNs were plated with approximately 8,000-10,000 neurons per aggregate, with micro-column lengths ranging from 2mm to 9mm; further, both unidirectional (with one aggregate) and bidirectional (with two aggregates at either end) µTENNs were plated with different lengths. Healthy axonal outgrowth was found across all aggregate µTENNs along the ECM core within the first few days *in vitro* through analysis of phase microscopy images (Figure 2). All aggregate µTENNs exhibited rapid axonal growth rates, peaking at 1101.8±81.1 microns/day within the $LE_{BI,9}$ group. In general, aggregate µTENNs displayed maximal growth at 3 days *in vitro* (DIV); exceptions included $LE_{BI,8}$ and $LE_{UNI,5}$, where the fastest growth was observed at 5 DIV, and $LE_{UNI,2}$, with an average maximum growth rate of 580±43.9 microns/day at 1 DIV (Figure 2F, Table 1). Comparatively, dissociated µTENNs exhibited a peak growth rate of 61.7±5 microns/day at 1 DIV, representing a nearly 17-fold reduction relative to the aggregate µTENNs within the $LE_{BI,9}$ group (Figure 2F, Table 1). Planar control cultures exhibited an average growth rate of 38.1±19.4 microns/day from 1 to 3 DIV and 39.1±20.6 microns/day from 3 to 5 DIV, after which single neurites could not be identified (Table 1). The two planar growth rates did not differ significantly, yielding a cumulative average growth rate of 38.6±20.0 microns/day.

One-way ANOVA of the average maximum growth rate identified a significant main effect of the LE group (F-statistic = 14.1, $p < 0.0001$). Subsequent Bonferroni analysis on pairwise comparisons revealed that the average maximum growth rates of bidirectional µTENNs ranging from 7 to 9 mm in length ($LE_{BI,7}$, $LE_{BI,9}$) were statistically higher than those 2 to 3 mm in length ($LE_{BI,2}$, $LE_{BI,3}$) ($p < 0.001$); additionally, the maximum growth rate of $LE_{BI,9}$ was found statistically higher than that of $LE_{UNI,2}$ ($p < 0.01$) and $LE_{UNI,5}$ ($p < 0.05$) (Figure 2). ANOVA of the minimum growth rate did not detect any differences across LE groups (F-statistic = 1.17, $p = 0.332$), while ANOVA of the average crossing time (F-statistic = 12.99, $p < 0.0001$) and Bonferroni post-hoc analysis showed that $LE_{BI,7}$ and $LE_{BI,9}$ axons crossed the length of the micro-column later than those of $LE_{UNI,2}$, $LE_{BI,2}$, $LE_{BI,3}$, and $LE_{BI,5}$ (Figure 2E). µTENNs within $LE_{UNI,5}$ did not, on average, fully span the construct length by 10 DIV (Figure 2, Table 1).

Growth Rates	$LE_{UNI,2}$	$LE_{BI,2}$	$LE_{BI,3}$	$LE_{UNI,5}$	$LE_{BI,5}$	$LE_{BI,7}$	$LE_{BI,9}$	$LE_{DISS,2}$	Planar
Initial	547±73.2	378±51.9	345±35.4	525±21.9	535±62.9	472±66.9	513±100.7	61.7±5.01	38.1±19.4
Maximum	580±43.9	453±33.8	559±28.7	656±88.3	838±43.2	894±79.2	1102±81.1	61.7±5.01	39.1±20.6
Minimum	430±73.0	248±22.7	324±38.0	202±74.9	395±56.4	336±57.4	313±68.3	-5.37±7.50	38.1±19.4
Crossing Time	4.33	3.60	3.67	NA	4.35	6.29	8.0	N/A	N/A

Table 1: µTENN Growth Characterization. Data presented as mean ± s.e.m. in units of microns/day (Initial, Maximum, and Minimum Growth Rates) and days in vitro (Crossing Time). LE subscripts indicate unidirectional (UNI), bidirectional (BI), or dissociated (DISS) µTENNs and the micro-column length in millimeters.

µTENN Viability

Neuronal survival was quantified via live/dead staining and confocal microscopy for short unidirectional and short bidirectional µTENNs at 10 and 28 DIV (Figure 3). Age-matched planar cultures served as controls. Percent viability was defined as the ratio of the summed area of calcein-AM-positive cells to that of all stained cells (i.e. both calcein-AM^+ and ethidium $homodimer^+$ cells). Neuronal survival in µTENNs was observed to persist up to at least 28 DIV, with further demonstration of survival out to 40 DIV (Figure 3). ANOVA showed that although the DIV was a significant main effect (F-statistic = 32.21, $p < 0.0001$), the LE/culture group was not a significant factor ($p > 0.84$). The interaction effect was significant ($p < 0.01$), so Bonferroni analysis was used to compare groups at each time point (Figure 3G). Viability of planar cultures at 28 DIV (53.6%) was found statistically lower than that of LE_{UNI} (80.3%) ($p < 0.05$), LE_{BI} (84.8%) ($p < 0.001$), and planar cultures (97.7%) ($p < 0.0001$) at 10 DIV.

Moreover, planar culture viability at 10 DIV surpassed those of both LE_{UNI} (68.1%) and LE_{BI} (69.0%) at 28 DIV ($p < 0.01$). Overall, planar cultures exhibited a 45% decline in viability from 10 to 28 DIV, while LE_{UNI} and LE_{BI} showed a 15.2% and 18.6% drop over time, respectively (Figure 3).

µTENN Architecture and Synaptogenesis

To characterize µTENN architecture, bidirectional µTENNs were either labeled with GFP and mCherry and imaged over time or fixed and immunolabeled at set timepoints to identify cell nuclei, axons, and synapses (Figure 4). Confocal images of GFP/mCherry µTENNs revealed that upon making contact with opposing axons, projections continued to grow along each other towards the opposing aggregate, confirming physical interaction and integration between the two neuronal populations (Figure 4). Immunolabeling revealed that neuronal somata were localized almost exclusively to the aggregates, which were spanned by long axons, as indicated with Tuj-1 (Figure 4H); axons and dendrites were also found within the aggregates from intra-aggregate connections, presumably formed upon or shortly after plating. Synapse presence was qualitatively assessed using the sum area of synapsin$^+$ puncta across the specified timepoints. A modest distribution of synapsin within µTENN aggregates was observed, as well as an increase in synapsin expression within the lumen of the micro-columns, suggesting that neurons within bidirectional µTENNs synaptically integrate and therefore have the capacity to communicate between aggregates.

Calcium Imaging and Optical Stimulation

Bidirectional µTENNs expressing the calcium reporter GCaMP6f exhibited spontaneous oscillations in the delta band (1-5 Hz) in the absence of external stimulation, with the synchronicity of oscillation between aggregates suggesting the potential formation of synaptic networks. Moreover, the introduction of the NMDA and AMPA receptor antagonists D-APV and CNQX to media containing bidirectional µTENNs reversibly abolished endogenous activity as measured by the calcium reporter GCaMP6f (data not shown), indicating that the calcium transients observed may reflect action potential firing due to synaptic transmission. Bidirectional µTENNs were also engineered to enable light-based stimulation and concurrent calcium imaging *in vitro* by transducing one aggregate with ChR2 and the opposing aggregate with RCaMP. Upon illumination of ChR2$^+$ (input) aggregates with 465nm light (stimulation wavelength of ChR2), the opposing RCaMP$^+$ (output) aggregates exhibited timed changes in fluorescence intensity in response. As a negative control, the input aggregate was exposed to 620nm light (off-target wavelength), revealing no readily observable responses; the mean peak $\Delta F/F_o$ of the output aggregate was significantly greater under 465nm stimulation than 620nm stimulation at 634mW/mm^2 ($p < 0.05$). Collectively, these findings suggest that the changes in $\Delta F/F_o$ under 465nm stimulation reflected synaptically mediated firing of neurons in the output aggregate in response to light-based activation of neurons within the input aggregate. Although there was high variability in $\Delta F/F_o$ between µTENNs, the percent change relative to baseline fluorescence due to optical stimulation could be reproducibly distinguished from endogenous activity across all the µTENNs studied and the average maximum $\Delta F/F_o$ positively correlated with the stimulation intensity (Figure 5). Overall, these results suggest that light-based stimulation of the input aggregate resulted in controllable signal propagation and modulation of activity in the output aggregate.

Implantation and Intravital Calcium Imaging

µTENNs – fabricated as described above and transduced to express GCaMP6 – were implanted as a proof-of-concept for living electrode survival, integration, and function. One week and one month-post injection in the rodent brain, constructs were found to have survived and maintained the preformed somatic-axonal architecture, with cell bodies predominantly localized to one or both micro-column terminals and spanned by axonal tracts (Figure 6). Large, dense clusters of GCaMP$^+$ cell bodies (aggregates) were found at the dorsal and ventral regions of implantation, with axons and dendrites within the lumen spanning the two locations (Figure 6). There was also significant neurite outgrowth from the ventral end of the living electrode, with structural evidence of synapse formation with host

neurons (Figure 6). In some cases, there was also neuronal migration up to several millimeters from the ventral implant location, although the presence and extent of migration varied across implants. Multiphoton imaging revealed GCaMP-positive µTENN neurons in V1 at both 5 and 10 days post-implant (Figure 7). The breathing of the anesthetized animal was controlled via monitoring and controlled isoflurane delivery, and changes in GCaMP fluorescence intensity due to breathing artifact were readily identified within the FFT of the time-lapse recordings as a ~0.5-0.7 Hz peak (Figure 7). Non-artifact changes in GCaMP intensity were present in the delta band (1-5 Hz), indicating µTENN survival and neuronal activity (Figure 7). Putative activity was also present at frequencies below 1 Hz, within the reported range reported for slow-wave cortical activity under anesthesia and during sleep[21,22]. Calcium recordings of µTENNs at both 5 and 10 days post-implant reflected those of non-implanted µTENNs at 10 DIV, which was also dominated by low frequency activity in the 1-5 Hz range (as shown in Figure 5).

Discussion

Microelectrodes—the current gold standard for recordings—have been deployed successfully on the order of months, and less frequently years, in rodents, non-human primates, and human patients[3,23–25]. However, microelectrode-based BCIs generally succumb to a complex combination of abiotic and biological factors, including neuronal loss/migration, gliosis, biofouling, electrode movement, and/or mechanical failure – which impede stability, specificity, and clinical deployment[3–8,26]. Optogenetic strategies for neuromodulation permit more selective stimulation, but must address formidable challenges such as restricting the vector of interest to targeted cells, addressing the scattering and limited tissue penetration of light, and activating transduced cells without overheating brain tissue[27–30]. Efforts to minimize inflammation have yielded more compliant electrodes and electrode coatings/co-factors; however, the chronic foreign body response, consequent signal drop, and increase in stimulation thresholds continue to affect many current systems.

As an alternative to conventional microelectrodes and/or optogenetics strategies, µTENNs as living electrodes may present a biohybrid BCI with improved selectivity and longevity. By being fully fabricated *in vitro*, µTENNs leverage advantages of optogenetics while (1) avoiding any inherent risks of introducing active viruses *in vivo*, (2) restricting viral expression to the µTENN neurons only, and (3) leveraging well-established stereotactic neurosurgical techniques. The micro-column size may be minimized to reduce the microinjection footprint, while its material properties (e.g. stiffness) and potential co-factors (e.g. anti-inflammatory/growth factor release) may be tailored against any subsequent foreign body response. Moreover, while the constructs in this study were predominantly glutamatergic, µTENNs may be seeded with other neuronal subtypes for various applications (e.g. inhibitory or dopaminergic neurons) to enable more targeted integration based on the synaptogenetic behaviors of the subtype. Finally, as the µTENN-brain interface is synaptic, living electrodes may potentially last for the patient's lifetime. Given the potential benefits of the µTENN paradigm, the work described here represents a critical foundation in developing these implantable, engineered neural networks into a viable neural interface.

We found that neuronal aggregate-based fabrication allowed for more standardized construct architecture and repeatable studies compared to single-cell suspensions. Notably, we found that aggregate-based µTENNs exhibited faster axonal growth and greater total axonal lengths than their dissociated counterparts. The observed growth rates for dissociated µTENNs were similar to those in planar cultures, which averaged nearly 40 µm/day over the first 3 days (Figure 2). This falls within the growth reported in literature for cortical axons, which have reached lengths of up to 100-1000 µm over 3 days in planar cultures[31,32]. However, the peak axonal growth rates that were measured from aggregates greatly exceeded those in planar counterparts and dissociated µTENNs by 2 orders of magnitude, or over 1000 µm/day. Although further investigation is needed, we have identified a few potential causes of this significant benchmark. First, the restriction of axonal outgrowth to the micro-

column interior resulted in the formation of "bundles" of axons from the aggregates, which may be directionally self-reinforcing and accelerate linear extension. Second, the lack of synaptic targets within the micro-column may reduce axon branching between aggregates, which would otherwise slow growth cone movement[31,33–36]. Further, although longer µTENNs generally exhibited faster growth than shorter ones, initial growth rates did not vary significantly across different lengths. Thus greater separation between the aggregates may be necessary to establish either sufficient chemotactic gradients or a "ramp up" of growth machinery, such that maximal growth rates are only reached when targets are several mm away. Finally, axon growth was mediated, if not accelerated, by the collagen-laminin ECM, as its constituents are known to support axonal growth[37]. Indeed, aggregate µTENNs created without ECM had limited neurite outgrowth and did not develop inter-aggregate connections (data not shown).

µTENN neuronal viability was shown to persist for up to 40 DIV, suggesting their potential for use in long-term *in vitro* studies. Interestingly, the decline in viability from 10 to 28 DIV was lower for both unidirectional and bidirectional µTENNs than for planar cultures. While the cause of this improved survival potential has not been fully investigated, established work suggests that neurons exhibit better growth and survival in three-dimensional environments, which more accurately approximate conditions *in vivo*[38]. Similarly, the anatomically inspired 3D microstructure of the neuronal aggregates and axonal bundles may enable neurons to better self-regulate and survive compared to 2D cultures.

In addition to rapid growth, structural evidence of neuritic and synaptic integration was visualized as early as 4 DIV within the micro-columns. As the primary points of contact and communication between neurons, synapses are often used to determine the functional maturity of neuronal cultures[39,40]. Synapsin$^+$ puncta were observed to increase between 4 DIV and 28 DIV, suggesting that µTENN neurons form functional connections soon after plating which mature and expand over time, consistent with literature for planar cortical cultures[40]. Future network connectivity studies may more fully characterize the development and distribution of intra- versus inter-aggregate synapses; however, it is likely that intra-aggregate synapses initially dominate the total synapse population before axons span the aggregates and enable inter-aggregate synapses to form. These analyses would build on the aggregate-specific labeling achieved here to distinguish structures from either aggregate (Figure 4). Overall, these results indicate that µTENNs are capable of quickly and consistently forming the desired µTENN architecture – important for the fabrication of clinically viable constructs – which is maintained over weeks *in vitro*. Moreover, the µTENNs' structure may make them an ideal system for studying neuronal growth, maturation, and network dynamics *in vitro*, with characteristics approximating the 3D architecture of connectome-spanning structures in the mammalian brain more closely than planar cultures[38].

Initially, we measured spontaneous activity in and across the aggregates (Figure 5, Supplemental Movies 1 & 2), which consisted primarily of delta oscillations (1-5 Hz). Concurrent network analyses have shown that µTENNs *in vitro* exhibit inter-aggregate synchronicity within the delta band[41]. The introduction of glutamatergic receptor blockers and subsequent suppression of GCaMP$^+$ activity implicate synaptic transmission as the primary contributor to changes in reporter fluorescence. Optical stimulation and recordings of evoked activity across aggregates further demonstrate the presence of functional synapses. Post-transplant, this activity persisted, along with slow-wave activity recorded below 1 Hz. Slow-wave oscillations have been recorded under anesthesia and during slow-wave sleep, as well as in cortical neuronal cultures *in vitro*[21,22]. Whether the <1 Hz activity observed within the µTENNs reflects cortical activity is unknown at present and will be further determined through continued intravital, functional, and histological analyses at longer timepoints. Combined with the presented histology, there is strong evidence that µTENNs survive post-transplant and form putative synapses with the cortex, although we observed significant overgrowth and integration with a subset of our transplants. As such, controllability over neuronal migration and the targeting of synaptic integration remains an ongoing design challenge that will need to be addressed to ensure proper function. This

may be done by controlling neuronal subtype as discussed, or by otherwise manipulating the transplant environment to promote more targeted integration, e.g. introducing or promoting expression of trophic factors implicated in axonal guidance and/or synaptic pruning during development[42,43]. Potential physical targeting methods include a porous membrane at the ventral terminal to restrict neuronal migration while permitting axonal projections between the µTENN and host brain.

In summary, we have created living electrodes – hydrogel-encapsulated neuronal populations linked by functional axonal tracts – and demonstrated their construction, functional validation, targeted delivery, and survival and integration post-transplant. These achievements lay the groundwork for more in-depth investigations of the translational utility of the µTENNs following targeted transplant in the cerebral cortex or other anatomical targets. Future work will assess the ability of transplanted µTENNs to modulate (input) and/or record (output) brain activity as a neural interface (Figure 1). For inputs, unidirectional, optogenetically-active µTENNs may bypass the light scattering and limited penetration depth of conventional optogenetic methods by relaying light stimulation at the cortical surface into synaptic inputs to the desired target. For outputs, bidirectional µTENNs may be transduced with $GCaMP^+$ or similar reporters and transplanted. Upon forming synapses with host neurons; $GCaMP^+$ µTENNs may be used to monitor neuronal activity deeper in the brain, transferring deeper neural signals into detectable fluorescent signals at the brain surface. Taken together, these results serve as an early proof-of-concept for µTENNs as a platform for biologically-based neuromodulation. Through optogenetic and tissue-engineering techniques, we have created a foundation for using preformed, implantable neural networks as a potentially long-term neural interface at the intersection of neuroscience and engineering.

Author Contributions:
Conceptualization: D.K.C., J.A.W., M.D.S., H.I.C.; Methodology: D.K.C., D.O.A., L.A.S., J.P.H., A.D.N., J.C.B., D.P., H.I.C., J.A.W.; Formal Analysis: D.O.A.; Investigation: D.O.A., J.C.B.; Resources: R.H.K.; Visualization: D.O.A.; Writing – Original Draft: D.O.A.; Writing – Review & Editing: D.O.A., D.K.C., L.A.S., J.P.H., A.D.N., J.C.B., D.P., R.H.K., H.I.C., J.A.W., M.D.S; Supervision: D.K.C., J.A.W., M.D.S., R.H.K., H.I.C.; Project Administration: D.K.C.; Funding Acquisition (primary): D.K.C.

Acknowledgements:
Financial support was primarily provided by the National Institutes of Health [BRAIN Initiative U01-NS094340 (Cullen), T32-NS043126 (Harris) & T32-NS091006 (Struzyna)] and the National Science Foundation [Graduate Research Fellowship DGE-1321851 (Adewole)], with additional support from the Penn Medicine Neuroscience Center (Cullen), American Association of Neurological Surgeons and Congress of Neurological Surgeons [Codman Fellowship in Neurotrauma and Critical Care (Petrov)], and the Department of Veterans Affairs [Merit Review I01-BX003748 (Cullen), Merit Review I01-RX001097 (Cullen), Career Development Award #IK2-RX001479 (Wolf) & Career Development Award #IK2-RX002013 (Chen)]. Any opinion, findings, and conclusions or recommendations expressed in this material are those of the authors(s) and do not necessarily reflect the views of the National Institutes of Health, National Science Foundation, or Department of Veterans Affairs.

References

1. Wolpaw, J. R. Brain–computer interface. *Encycl. Neurosci.* 429–437 (2009). doi:10.1016/B978-008045046-9.01303-6
2. Wolpaw, J. R. *Brain-computer interfaces*. *Handbook of Clinical Neurology* **110,** (Elsevier B.V., 2013).
3. Adewole, D. O., Serruya, M. D., Harris, J. P., Burrell, J. C., Petrov, D., Chen, H. I., Wolf, J. A. & Cullen, D. K. The evolution of neuroprosthetic interfaces. *Crit. Rev. Biomed. Eng.* **44,** 123–152 (2016).
4. Tresco, P. A. & Winslow, B. D. The challenge of integrating devices into the central nervous system. *Crit. Rev. Biomed. Eng.* **39,** 29–44 (2011).
5. Harris, J. P. & Tyler, D. J. Biological, mechanical, and technological considerations affecting the longevity of intracortical electrode recordings. *Crit. Rev. Biomed. Eng.* **41,** 435–56 (2013).
6. Grill, W. M., Norman, S. E. & Bellamkonda, R. V. Implanted neural interfaces: biochallenges and engineered solutions. *Annu. Rev. Biomed. Eng.* **11,** 1–24 (2009).
7. McConnell, G. C., Rees, H. D., Levey, A. I., Gutekunst, C.-A., Gross, R. E. & Bellamkonda, R. V. Implanted neural electrodes cause chronic, local inflammation that is correlated with local neurodegeneration. *J. Neural Eng.* **6,** 056003 (2009).
8. Polikov, V. S., Tresco, P. a. & Reichert, W. M. Response of brain tissue to chronically implanted neural electrodes. *J. Neurosci. Methods* **148,** 1–18 (2005).
9. Cogan, S. F. Neural stimulation and recording electrodes. *Annu. Rev. Biomed. Eng.* **10,** 275–309 (2008).
10. Aravanis, A. M., Wang, L.-P., Zhang, F., Meltzer, L. a, Mogri, M. Z., Schneider, M. B. & Deisseroth, K. An optical neural interface: in vivo control of rodent motor cortex with integrated fiberoptic and optogenetic technology. *J. Neural Eng.* **4,** S143–S156 (2007).
11. Pashaie, R., Anikeeva, P., Lee, J. H., Prakash, R., Yizhar, O., Prigge, M., Chander, D., Richner, T. J. & Williams, J. Optogenetic brain interfaces. *IEEE Rev. Biomed. Eng.* **7,** 3–30 (2014).
12. Fan, B. & Li, W. Miniaturized optogenetic neural implants: a review. *Lab Chip* **15,** 3838–55 (2015).
13. Harris, J. P., Struzyna, L. A., Murphy, P. L., Adewole, D. O., Kuo, E. & Cullen, D. K. Advanced biomaterial strategies to transplant preformed micro-tissue engineered neural networks into the brain. *J. Neural Eng.* **13,** 016019 (2016).
14. Struzyna, L., Wolf, J., Mietus, C., Chen, I. H., Smith, D. H., Cullen, D. K., Chen, H. I., Smith, D. H. & Cullen, D. K. Rebuilding brain circuitry with living micro-tissue engineered neural networks. *Tissue Eng.* **21,** 2744–2756 (2015).
15. Struzyna, L. A., Harris, J. P., Katiyar, K. S., Chen, H. I. & Cullen, D. K. Restoring nervous system structure and function using tissue engineered living scaffolds. *Neural Regen. Res.* **10,** 679–685 (2015).
16. Struzyna, L. A., Adewole, D. O., Gordián-Vélez, W. J., Grovola, M. R., Burrell, J. C., Katiyar, K. S., Petrov, D., Harris, J. P. & Cullen, D. K. Anatomically inspired three-dimensional micro-tissue engineered neural networks for nervous system reconstruction, modulation, and modeling. *J. Vis. Exp. JoVE* (2017). doi:10.3791/55609
17. Ungrin, M. D., Joshi, C., Nica, A., Bauwens, C. & Zandstra, P. W. Reproducible, ultra high-throughput formation of multicellular organization from single cell suspension-derived human

embryonic stem cell aggregates. *PLoS One* **3,** (2008).

18. Akerboom, J., Carreras Calderón, N., Tian, L., Wabnig, S., Prigge, M., Tolö, J., Gordus, A., Orger, M. B., Severi, K. E., Macklin, J. J., Patel, R., Pulver, S. R., Wardill, T. J., Fischer, E., Schüler, C., Chen, T., Sarkisyan, K. S., Marvin, J. S., Bargmann, C. I., Kim, D. S., Kügler, S., Lagnado, L., Hegemann, P., Gottschalk, A., Schreiter, E. R. & Looger, L. L. Genetically encoded calcium indicators for multi-color neural activity imaging and combination with optogenetics. *Front. Mol. Neurosci.* **6,** 2 (2013).

19. Patel, T. P., Man, K., Firestein, B. L. & Meaney, D. F. Automated quantification of neuronal networks and single-cell calcium dynamics using calcium imaging. *J. Neurosci. Methods* **243,** 26–38 (2015).

20. Mank, M., Santos, A. F., Direnberger, S., Mrsic-Flogel, T. D., Hofer, S. B., Stein, V., Hendel, T., Reiff, D. F., Levelt, C., Borst, A., Bonhoeffer, T., Hübener, M. & Griesbeck, O. A genetically encoded calcium indicator for chronic in vivo two-photon imaging. *Nat. Methods* **5,** 805–811 (2008).

21. Franken, P., Dijk, D. J., Tobler, I. & Borbely, A. A. Sleep-deprivation in rats - effects on eeg power spectra, vigilance states, and cortical temperature. *Am. J. Physiol.* **261,** R198–R208 (1991).

22. Steriade, M., Nuñez, a & Amzica, F. A novel slow (< 1 hz) oscillation of neocortical neurons in vivo: depolarizing and hyperpolarizing components. *J. Neurosci.* **13,** 3252–3265 (1993).

23. Hochberg, L. R., Serruya, M. D., Friehs, G. M., Mukand, J. a, Saleh, M., Caplan, A. H., Branner, A., Chen, D., Penn, R. D. & Donoghue, J. P. Neuronal ensemble control of prosthetic devices by a human with tetraplegia. *Nature* **442,** 164–171 (2006).

24. Gilja, V., Pandarinath, C., Blabe, C. H., Nuyujukian, P., Simeral, J. D., Sarma, A. a, Sorice, B. L., Perge, J. a, Jarosiewicz, B., Hochberg, L. R., Shenoy, K. V & Henderson, J. M. Clinical translation of a high-performance neural prosthesis. *Nat. Med.* **21,** 6–8 (2015).

25. Krüger, J., Caruana, F., Volta, R. D. & Rizzolatti, G. Seven years of recording from monkey cortex with a chronically implanted multiple microelectrode. *Front. Neuroeng.* **3,** 6 (2010).

26. Prasad, A., Xue, Q.-S., Sankar, V., Nishida, T., Shaw, G., Streit, W. J. & Sanchez, J. C. Comprehensive characterization and failure modes of tungsten microwire arrays in chronic neural implants. *J. Neural Eng.* **9,** 056015 (2012).

27. Towne, C., Montgomery, K. L., Iyer, S. M., Deisseroth, K. & Delp, S. L. Optogenetic control of targeted peripheral axons in freely moving animals. *PLoS One* **8,** (2013).

28. Scharf, R., Tsunematsu, T., Mcalinden, N., Dawson, M. D., Sakata, S. & Mathieson, K. Depth-specific optogenetic control in vivo with a scalable , high-density µ led neural probe. *Nat. Publ. Gr.* 1–10 (2016). doi:10.1038/srep28381

29. Llewellyn, M. E., Thompson, K. R., Deisseroth, K. & Delp, S. L. Orderly recruitment of motor units under optical control in vivo. *Nat. Med.* **16,** 1161–1165 (2010).

30. Favre-Bulle, I. a, Preece, D., Nieminen, T. a, Heap, L. a, Scott, E. K. & Rubinsztein-Dunlop, H. Scattering of sculpted light in intact brain tissue, with implications for optogenetics. *Sci. Rep.* **5,** 11501 (2015).

31. Szebenyi, G., Callaway, J. L., Dent, E. W. & Kalil, K. Interstitial branches develop from active regions of the axon demarcated by the primary growth cone during pausing behaviors. *J. Neurosci.* **18,** 7930–7940 (1998).

32. Meberg, P. J. & Miller, M. W. Culturing hippocampal and cortical neurons. *Methods Cell Biol.* **71,**

111–127 (2003).

33. Kalil, K., Szebenyi, G. & Dent, E. W. Common mechanisms underlying growth cone guidance and axon branching. *J. Neurobiol.* **44,** 145–158 (2000).

34. Halloran, M. C. & Kalil, K. Dynamic behaviors of growth cones extending in the corpus callosum of living cortical brain slices observed with video microscopy. *J. Neurosci.* **14,** 2161–2177 (1994).

35. Tang, F., Dent, E. W. & Kalil, K. Spontaneous calcium transients in developing cortical neurons regulate axon outgrowth. *J. Neurosci.* **23,** 927–936 (2003).

36. Kalil, K., Li, L. & Hutchins, B. I. Signaling mechanisms in cortical axon growth, guidance, and branching. *Front. Neuroanat.* **5,** 1–15 (2011).

37. Goldberg, J. L. How does an axon grow? *Genes Dev.* **17,** 941–958 (2003).

38. LaPlaca, M. C., Vernekar, V. N., Shoemaker, J. T. & Cullen, D. K. Three-dimensional neuronal cultures. *Methods Bioeng. 3d Tissue Eng.* 187–204 (2010).

39. Harrill, J. A., Chen, H., Streifel, K. M., Yang, D., Mundy, W. R. & Lein, P. J. Ontogeny of biochemical, morphological and functional parameters of synaptogenesis in primary cultures of rat hippocampal and cortical neurons. *Mol. Brain* **8,** 10 (2015).

40. Cullen, D. K., Gilroy, M. E., Irons, H. R. & Laplaca, M. C. Synapse-to-neuron ratio is inversely related to neuronal density in mature neuronal cultures. *Brain Res.* **1359,** 44–55 (2010).

41. Dhobale, A. V., Adewole, D. O., Ho, A., Chan, W., Marinov, T. & Mijail, D. Assessing functional connectivity across three-dimensional tissue engineered axonal tracts using calcium fluorescence imaging. (Submitted for publication) (2018).

42. Vanderhaeghen, P. & Cheng, H.-J. Guidance molecules in axon pruning and cell death. *Cold Spring Harb. Perspect. Biol.* **2,** (2010).

43. Low, L. K. & Cheng, H.-J. Axon pruning: an essential step underlying the developmental plasticity of neuronal connections. *Philos. Trans. R. Soc. B Biol. Sci.* **361,** 1531–1544 (2006).

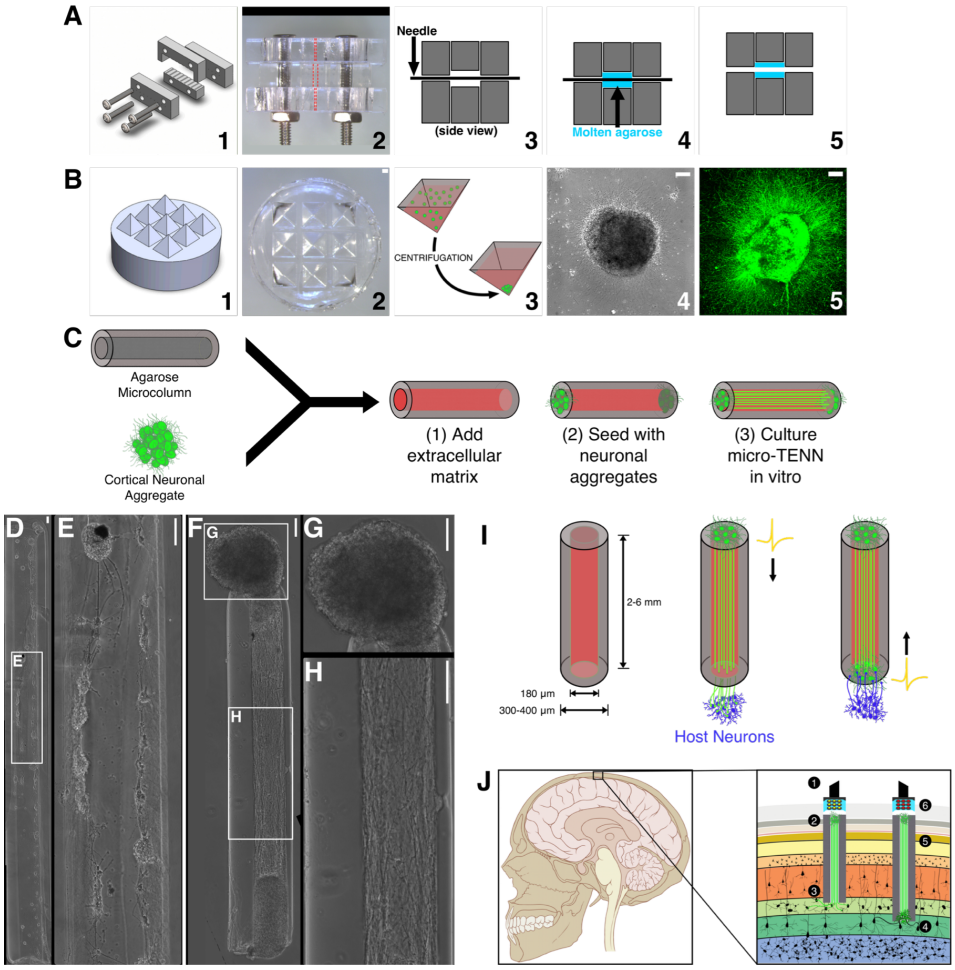

Figure 1: µTENN Fabrication and Living Electrode Concept. µTENNs comprise a hydrogel micro-column, living neuronal aggregates, and an extracellular matrix lumen. **(A) 1**: A customizable acrylic mold for generating micro-columns. **2**: Top view of the mold (dashed lines represent outer and inner diameters). **3**: Needles of the desired inner diameter are inserted into the mold. **4**: Molten agarose (blue) is introduced into the mold and cooled. **5**: Micro-columns are removed after needle removal/mold disassembly. **(B) 1**: A 3D-printed mold for square pyramidal wells. **2**: Pyramidal wells cast in PDMS. **3**: Dissociated neurons (green) forced into aggregates through centrifugation. **4**: Phase image of an aggregate 24 hours after plating. **5**: Confocal reconstruction of aggregate at 72 hours, labeled with GFP. **(C)** Micro-columns (gray) are filled with an extracellular collagen-laminin matrix (red). Neuronal aggregates are then placed at one or both ends of the micro-column and grown *in vitro*. **(D)** µTENNs were originally fabricated with dissociated neurons, yielding limited control over axonal growth and network formation **(E)**. Aggregate µTENNs **(F)** exhibit robust axonal growth and more controllable architecture, with discrete regions of cell bodies **(G)** and neuritic projections **(H)**. **(I)** Left: Current µTENN dimensions. Middle: Unidirectional µTENNs synapse host neurons (purple) to relay inputs to targeted cortical regions. Right: Host neurons synapse bidirectional µTENNs, relaying activity from host cortex to the dorsal aggregate. **(J)** µTENNs as transplantable input/output channels. *Inputs*: an LED array (1) optically stimulates a unidirectional, channelrhodopsin-positive µTENN (2) to activate Layer IV neurons (3). *Outputs*: Layer V neurons (4) synapse a bidirectional µTENN (5); relayed neuronal activity is recorded by a microelectrode array (6). Scale bars: 100 µm.

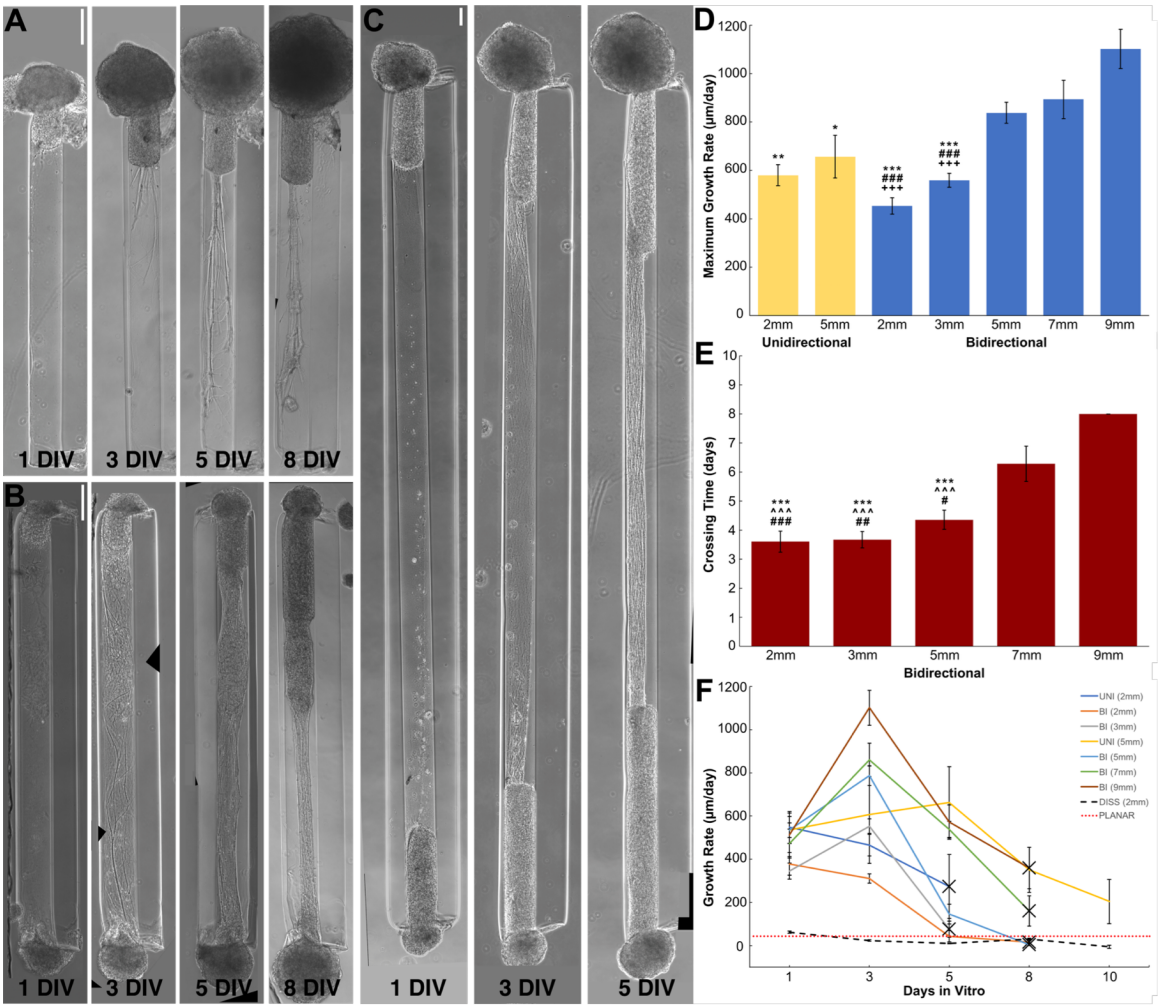

Figure 2: Axonal Growth in Aggregate µTENNs Over Time. Both unidirectional **(A)** and bidirectional **(B)** µTENNs displayed robust axonal outgrowth along the ECM core. While outgrowth within unidirectional µTENNs peaked within the first 3 DIV before declining, bidirectional µTENN axons crossed the length of the micro-column, synapsing with the opposing aggregate by 5 DIV. Representative 2mm µTENNs shown at 1, 3, 5, and 8 DIV. **(C)** Longer bidirectional µTENNs (5 mm) took more time to develop, but still showed robust growth. Representative 5mm µTENN shown at 1, 3, and 5 DIV. **(D)** Average maximum growth rates across µTENN groups. Symbols denote significant differences vs. 9mm bidirectional (*), 7mm bidirectional (#), and 5mm bidirectional (+) µTENNs, respectively. Symbol count denotes significance level (1: $p < 0.05$; 2: $p < 0.01$; 3: $p < 0.001$). **(E)** Average crossing times across µTENN groups. 5mm unidirectional µTENNs did not fully cross by 10 DIV and were not included. Symbols and symbol counts match those described in (D), with the addition of significance vs. 8mm bidirectional (^). **(F)** Growth rates for unidirectional, bidirectional, and dissociated/traditional µTENNs at 1, 3, 5, 8, and 10 DIV; dashed red line represents the average growth rate for planar cultures. Growth rates were quantified by identifying the longest neurite from an aggregate in phase microscopy images (10X magnification) at the listed timepoints. Crosses indicate axons crossing the length of the micro-column (unidirectional) or connecting between aggregates (bidirectional). Error bars denote s.e.m. Scale bars: 200 µm.

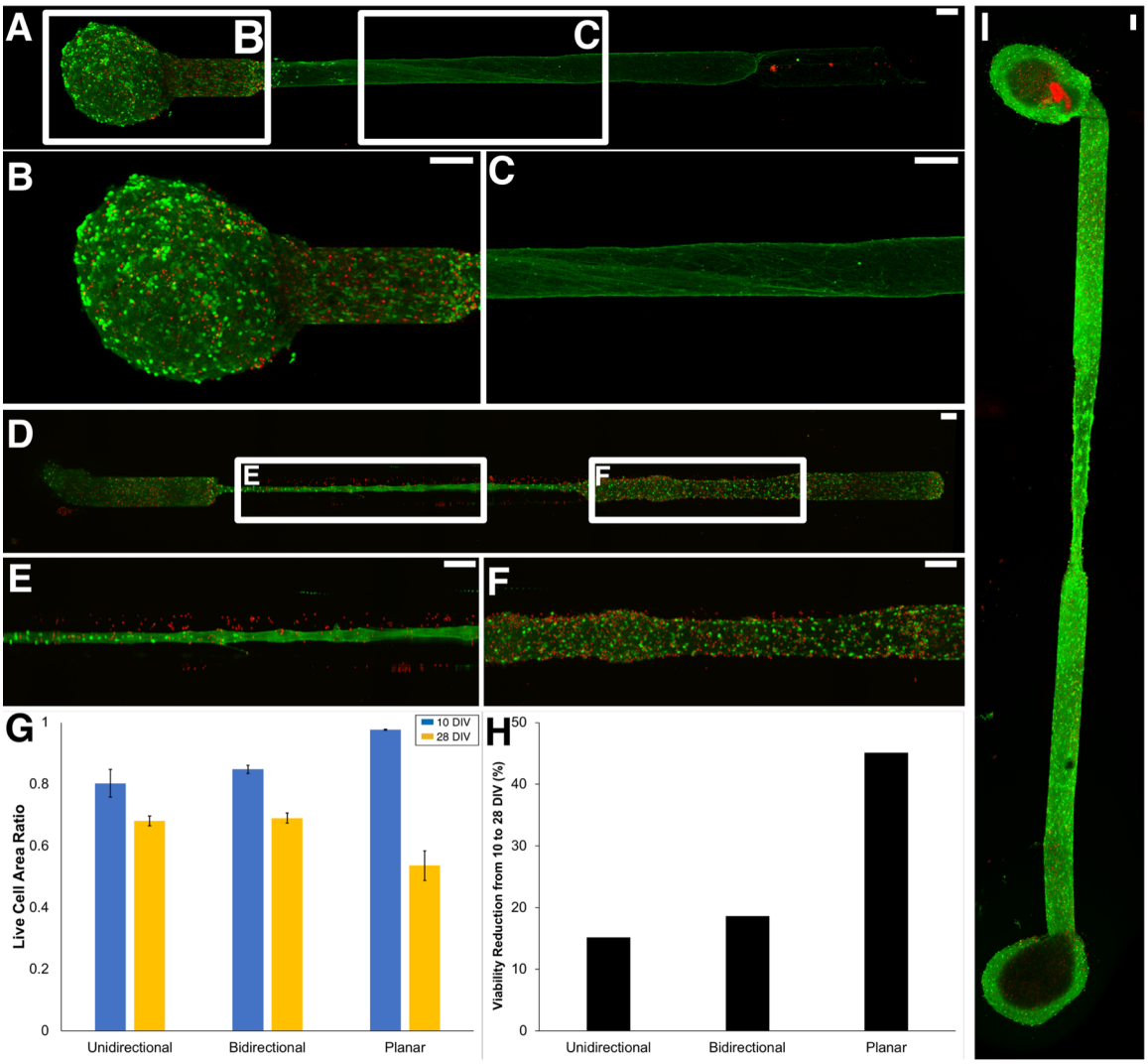

Figure 3: μTENN Viability. Viability for unidirectional and bidirectional μTENNs and age-matched two-dimensional controls was quantified via live-dead (calcein-AM/ethidium homodimer) staining at 10 and 28 DIV. **(a, b, c)** Representative confocal live-dead images showing live cells (green), dead cells (red), and an overlay of a unidirectional μTENN at 10 DIV, with outlined insets below. **(d, e, f)** Representative confocal live-dead image of a bidirectional μTENN at 28 DIV, with outlined insets below. **(G)** The average proportion of live to total (live + dead) cell body area for each experimental group and timepoint. Two-way ANOVA and post-hoc analysis revealed several statistically relevant pairwise differences (* = $p < 0.05$; ** = $p < 0.01$; *** = $p < .001$). Symbols denote significant differences vs. planar cultures at 10 DIV (#) and 28 DIV (*). Error bars denote s.e.m. Sample sizes: n = 4 and 4 (unidirectional); 7 and 4 (bidirectional); 9 and 5 (controls) for 10 and 28 DIV, respectively. **(H)** The percent change in viability across experimental groups. All groups showed a decline in viability, with the planar cultures nearing a three-fold drop in viability relative to the μTENNs. **(I)** Live-dead stain of a μTENN at 40 DIV. Scale bars: 100 μm.

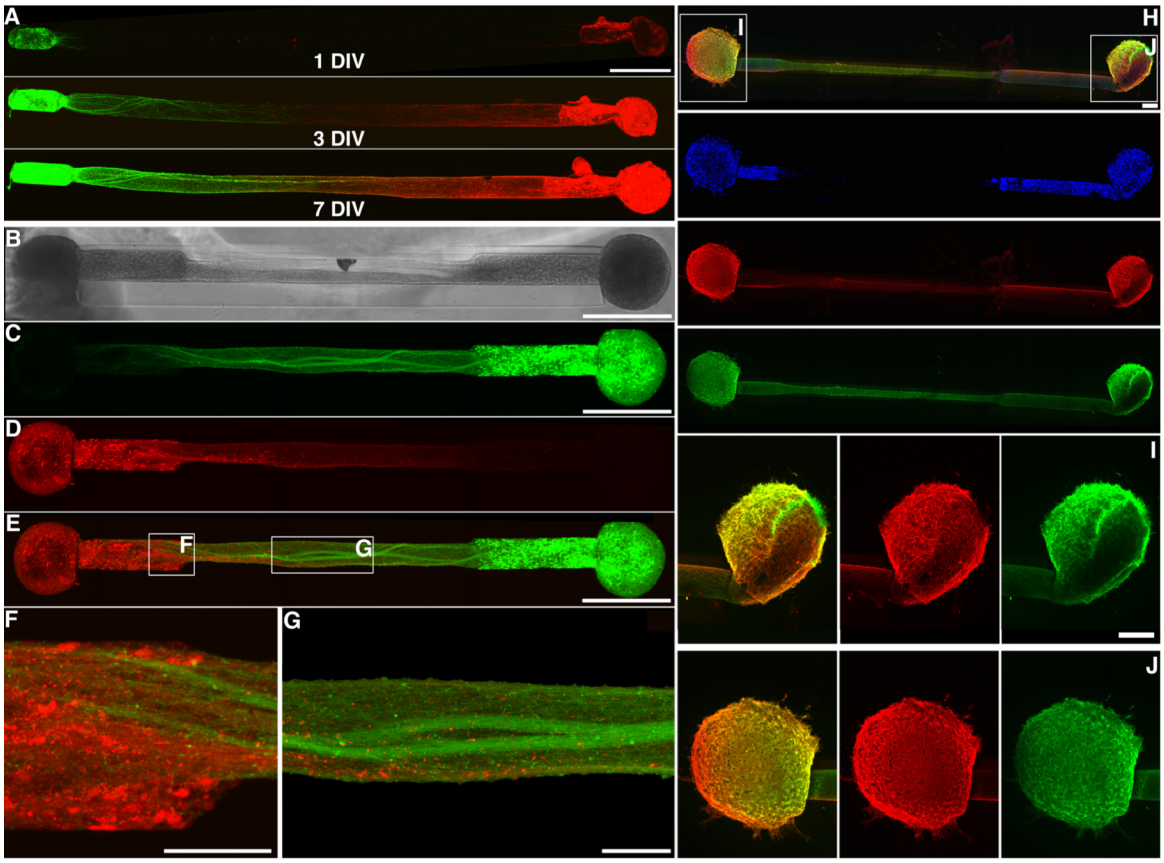

Figure 4: µTENN Growth and Architecture. Bidirectional µTENNs were labeled with GFP (green) and mCherry (red) to observe aggregate-specific axonal growth and structure *in vitro*. **(A)** Confocal reconstructions of a bidirectional, GFP/mCherry-labeled µTENN at 1, 3 and 7 DIV. **(B)** Phase image of a bidirectional, GFP/mCherry-labeled µTENN at 5 DIV. **(C-E)** Confocal reconstruction of the µTENN from (B) at 7 DIV, with insets showing axons from each aggregate growing along each other **(F)** and axons from one aggregate making contact with the opposite population **(G)**. **(H)** Confocal reconstruction of a representative bidirectional µTENNs at 10 DIV immunolabeled for cell nuclei (Hoechst; blue), axons (Tuj-1; red), and synapses (synapsin; green). Insets in (H) refer to callout boxes **(I)** and **(J)** showing zoom-ins of synapses, axonal networks, and the overlay of the two. Scale bars: 500 µm (A, B, C, E); 100 µm (F, G); 200 µm (H, I).

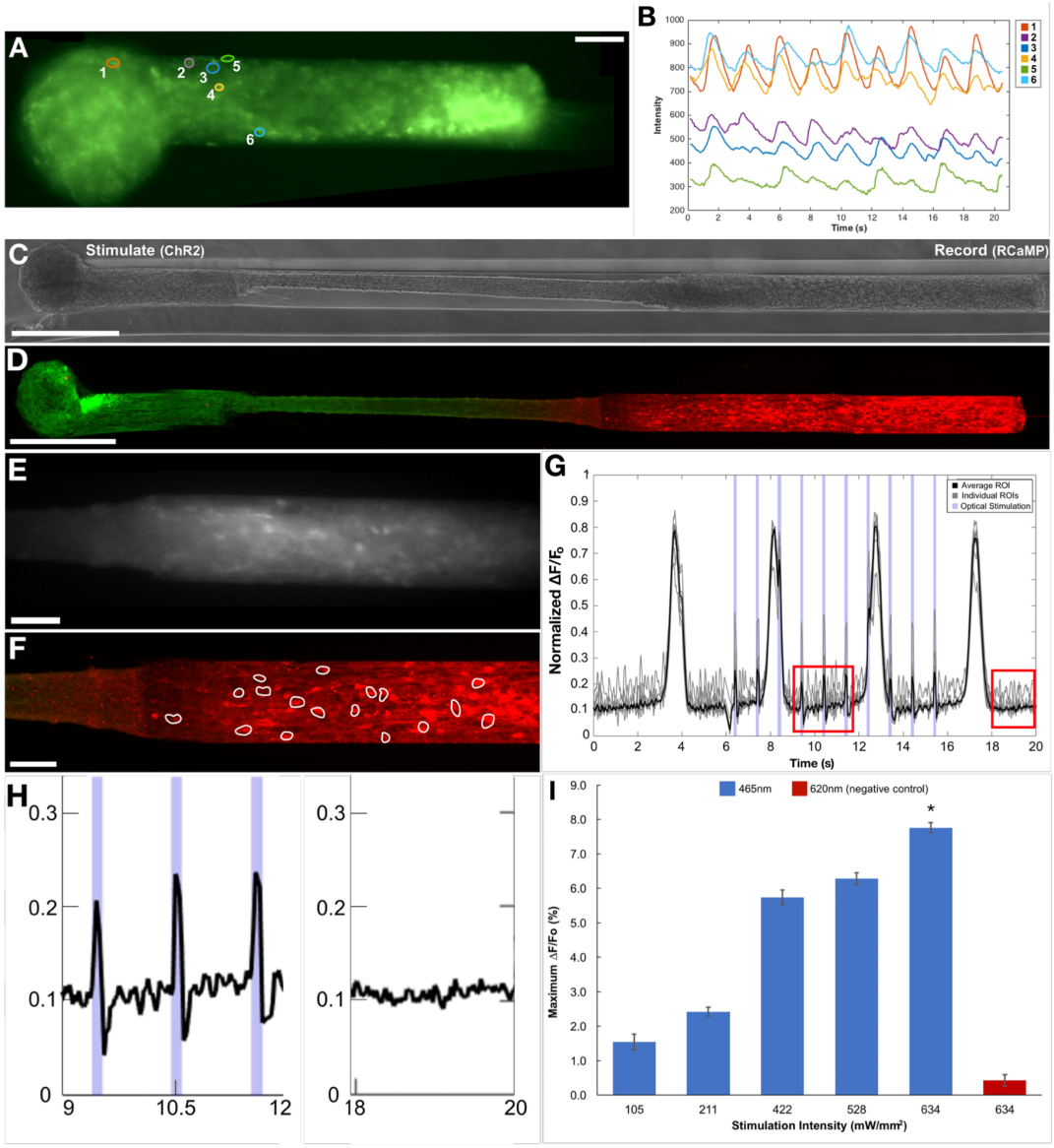

Figure 5: Simultaneous Optical Stimulation and Recording in µTENNs. µTENNs transduced to express both an optical actuator and a fluorescent calcium reporter may be controlled and monitored with light. **(A)** Representative micro-TENN transduced with GCaMP6 at 10 DIV. **(B) I**ntensities of the ROIs from (A) recorded over time. Intensities shown are normalized to the average of a background region (i.e. away from the micro-TENN). **(C)** Phase image and **(D)** confocal reconstruction of a µTENN at 10 DIV *in vitro*, with the left aggregate transduced with ChR2 and the right aggregate transduced with the calcium reporter RCaMP. **(E)** The RCaMP-positive aggregate from (D) under fluorescent microscopy during recording (16 fps). **(F)** Confocal reconstruction of (D) post-stimulation. ROIs containing single neurons were manually defined (white outlines). **(G)** Normalized pixel intensity of ROIs within the RCaMP+ aggregate from (a-c) during stimulation. Grey lines indicate representative, user-defined ROIs randomly selected for analysis, which were averaged to obtain a mean ROI of the aggregate (solid black line). The timestamps of a single train of 1 Hz, 100ms stimulation pulses are shown as blue bands along the abscissa. The changes in pixel intensity due to stimulation of the input aggregate can be seen as sharp spikes occurring within the endogenous, large-amplitude slow-wave activity. **(H)** Zoom-ins of the red insets from (G) showing µTENN activity during (left) stimulation and after (right) optical stimulation. **(I)** Average maximum $\Delta F/F_o$ across stimulation intensities. Although the maximum $\Delta F/F_o$ trended upward, the differences were not significant across intensities. Statistical comparison revealed that stimulation with the control wavelength (620nm) yielded significantly lower maximum $\Delta F/F_o$ than with 465nm (* = $p < 0.05$). Scale bars: 100 µm.

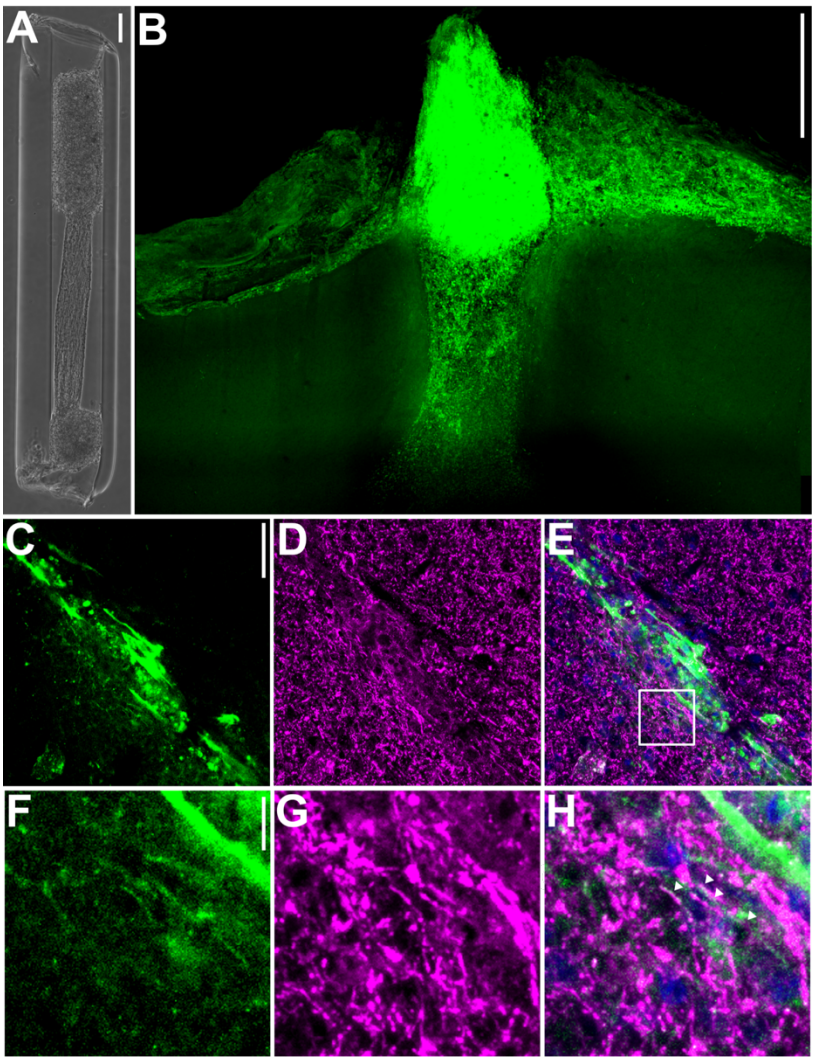

Figure 6: Living Electrode Survival and Integration *in Vivo*. (A) Phase image of a bidirectional µTENN prior to implantation; aggregates have been internalized to the micro-column. **(B)** Multiphoton image of the µTENN from (A) at one-month post-implant, showing GCaMP-positive µTENN neurons and processes within and immediately surrounding the construct. At one month, the dorsal aggregate had descended into the micro-column, suggesting externalized aggregates may be required to maintain a cohesive neuronal population at the surface. **(C-E)** Confocal image of a µTENN at one-month post implant, with synapsin^{+} puncta at and around the µTENN/brain interface. Shown are µTENN neurons (GFP; green), synapses (synapsin; purple) and nuclei (Hoechst, blue). **(F-H)** Zoom-ins of inset from (E) with colocalization of synapsin and GFP suggesting synaptic integration. Scale bars: 500 µm (B); 100 µm (A); 50 µm (C); 10 µm (F).

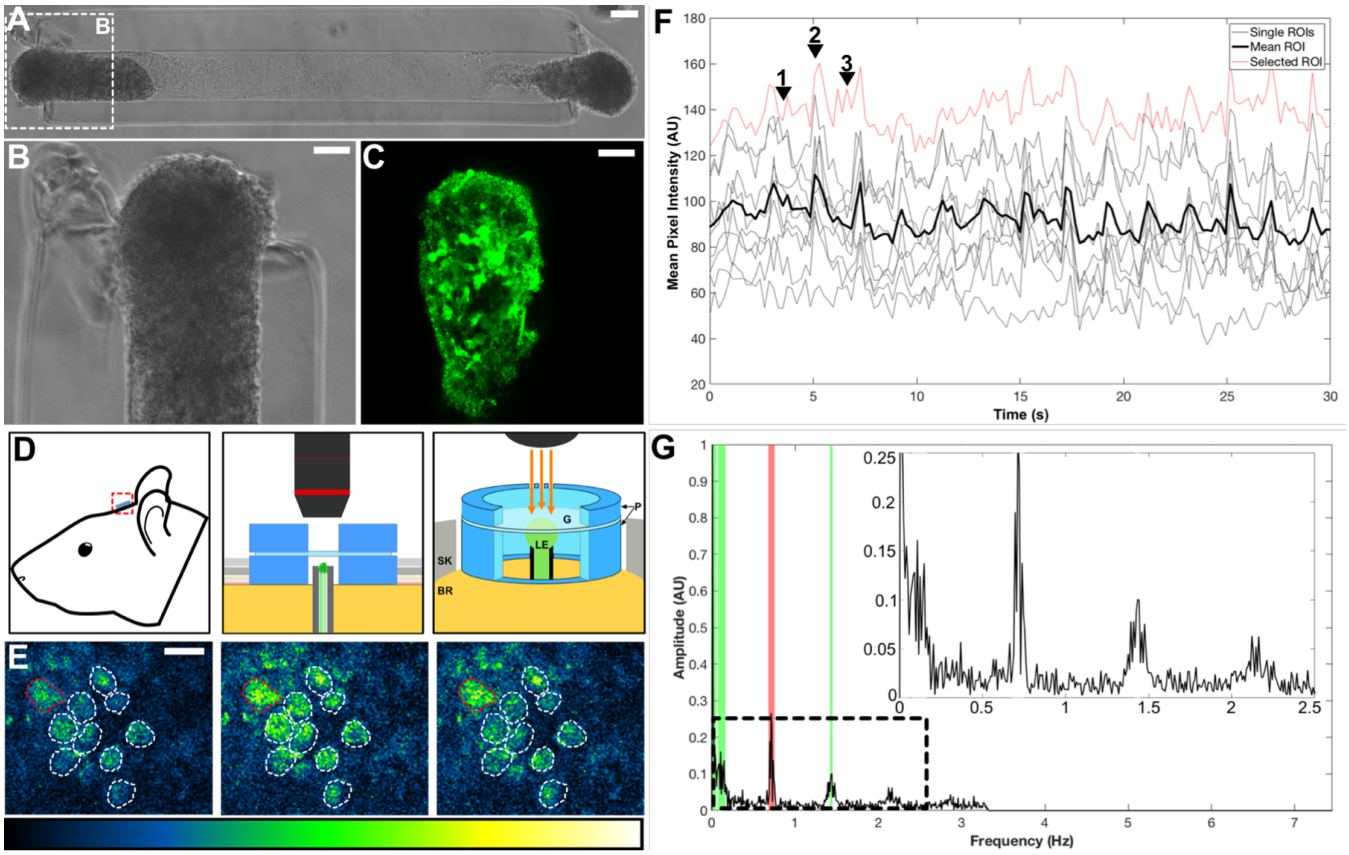

Figure 7: **Living Electrode Function *in Vivo*. (A)** Phase image of a GCaMP+ µTENN prior to implant. Inset refers to **(B)** showing the dorsal aggregate. **(C)** Multiphoton image of the dorsal aggregate of the µTENN, acquired immediately post-implant. **(D)** Conceptual schematic of the µTENN and cranial window. Inset shows in more detail the PDMS rings (P) sized to the skull craniotomy (SK) securing the glass coverslip (G) and protecting the implanted µTENN and underlying brain (BR), which may then be imaged chronically (orange arrows). **(E)** Single frames from multiphoton recording of the µTENN from (a-b) at 10 days post-implant during low activity (left), breathing (middle), and non-artifact neuronal activity (right). ROIs approximating single neurons are outlined. The LUTs scale (0-4096) is provided below. **(F)** Time course of calcium fluorescence from (E), showing the individual ROIs (grey/red) and average fluorescence across the aggregate. The red trace represents the ROI outlined in red in (E). Numbered arrows denote timestamps from (E). A sample of the recording can be found in Supplemental Video 3. **(G)** Fourier transform of the data from (F), showing spectral peaks due to the breathing rate as measured during imaging (red) and neuronal activity (green). Inset shows low-frequency activity similar to that observed *in vitro*. Scale bars: 100 µm (A); 50 µm (B, C); 20 µm (E).

Supplemental Videos 1 & 2: Calcium Imaging within µTENNs.
The two videos show spontaneous network activity within µTENN aggregates, visualized with the genetically encoded calcium reporter GCaMP6f. Video 1 shows the same µTENN aggregate shown in Figure 6E. Video 2 shows a bidirectional µTENN approximately 1.1mm in length, imaged at 10 days in vitro. Note that GCaMP activity can be seen in both the aggregate and axonal regions of the µTENN.

Supplemental Video 3: Simultaneous Optical Stimulation and Recording.
This video shows the $RCaMP^{+}$ aggregate of a ChR2/RCaMP µTENN approximately 6mm in length, imaged at 10 DIV during an optical stimulation/recording experiment. Red arrows indicate optical stimulation of the $ChR2^{+}$ aggregate outside of the field of view.